Research Article

Enhanced Crystallinity, Bandgap Modulation, and Charge Carrier Dynamics in Thermally Decomposed $Zn_xNi_{(1-x)}Fe_2O_4$

Phongsaphat Rangdee, Pimjai Saengkwamsawang, Anurak Prasatkhetragarn, and Arrak Klinbumrung*
Division of Physics, School of Science, University of Phayao, Phayao, Thailand

Wachirapun Juntrakul and Sakda Koenrobket
Division of Laboratory Operations, School of Science, University of Phayao, Phayao, Thailand

* Corresponding author. E-mail: Arrak.kl@up.ac.th DOI: 10.14416/j.asep.2025.11.007
Received: 13 June 2025; Revised: 18 August 2025; Accepted: 17 September 2025; Published online: 18 November 2025

Abstract
This study investigates the crystallographic and electronic modifications induced by zinc doping in $NiFe_2O_4$ ferrites, $Zn_xNi_{(1-x)}Fe_2O_4$, which are synthesized through a sustainable thermal decomposition. Although $NiFe_2O_4$ is extensively studied for optoelectronic and catalytic applications, its performance is limited by defect-related charge recombination and conductivity. Here, the crystallographic and electronic properties are tailored through controlled Zn incorporation. By varying the zinc concentrations from x = 0 to 0.09, the samples were examined for their structural, optical, and charge transport behaviors using X-ray diffraction (XRD), photoluminescence (PL), ultraviolet-visible (UV-Vis) spectroscopy, and impedance analysis. At x = 0.03, crystallinity is enhanced, defect density is minimized, and charge carrier mobility is significantly improved. The bandgap narrowed from 1.62 eV (undoped) to 1.43 eV (x = 0.07), and resistance dropped from 1.507×10^5 Ω to 0.378×10^5 Ω, indicating better charge transportation. The results suggest that moderate Zn doping modifies the cation distribution and promotes defect stabilization, enabling enhanced visible-light absorption and improved electrical behavior. This study confirms the benefits of defect engineering through thermal decomposition, further work is necessary to evaluate long-term stability, magnetic properties, and integration for specific applications. Challenges still exist in optimizing multi-dopant systems for device-scale deployment.

Keywords: Crystallography, $NiFe_2O_4$, Optical characteristics, Thermal decomposition process, Zn dopant

1 Introduction

Nickel ferrite ($NiFe_2O_4$) is a spinel ferrite material in which Fe^{3+} ions occupy both tetrahedral (A) and octahedral (B) sites, while Ni^{2+} ions are found in the octahedral sites [1], [2]. This specific cation distribution imparts unique magnetic, catalytic, and electrical properties, making it highly valuable for applications such as photoelectric devices, sensors, magnetic pigments, photocatalysts, and bone tissue engineering [3]–[5]. The properties of $NiFe_2O_4$ can be tailored by doping with transition metal ions, enabling advances in technology. The synthesis route and conditions significantly influence ferrites' structure and function. Traditional sol-gel, co-precipitation, and auto-combustion methods are employed to synthesize $NiFe_2O_4$ nanoparticles, allowing control over particle size, morphology, and phase composition. However, they have limitations like chemical waste, complex procedures, and scalability issues. Additionally, achieving high phase purity typically requires prolonged calcination at high temperatures, resulting in increased energy consumption. Thermal decomposition has emerged as a promising alternative for synthesizing spinel ferrites, offering scalability, environmental friendliness, and simplicity [6]. Although it has potential, thermal decomposition is still underused in creating defect-engineered ferrites with specific optical and electrical features.

Despite its advantages, the optoelectronic performance of $NiFe_2O_4$ is still hindered by intrinsic defects and limited charge carrier mobility. To enhance

photo-responsive activities, employing a metal oxide composite constitutes an effective strategy [7]. Additionally, doping with divalent ions, such as Zn^{2+}, effectively improves the structural and functional properties of spinel ferrites. Zn^{2+}, with its larger ionic radius (0.74 Å) compared to Ni^{2+} (0.69 Å), can create lattice distortions and modify the cation distribution between tetrahedral and octahedral sites [4]. As observed in previous studies, Zn doping has affected the magnetic and structural properties of $NiFe_2O_4$. The lattice constant increases with higher Zn levels, indicating a uniform distribution of Zn ions within the lattice [8]. The material's photocatalytic efficiency improves with Zn doping, resulting in substantial degradation of methylene blue dye under visible light [9]. Nevertheless, the effects of zinc doping on defect formation, charge carrier dynamics, and optical properties, particularly for materials synthesized via thermal decomposition, remain insufficiently studied. Additionally, the role of defect engineering in improving photoactivities and optoelectronic performance remains unclear, especially in the context of thermally processed systems.

This study investigated the structural, optical, and electrical modifications of $Zn_xNi_{(1-x)}Fe_2O_4$ (x = 0–0.09) synthesized through thermal decomposition. The result not only investigates the optoelectronic potential of Zn-doped $NiFe_2O_4$ but also emphasizes the unique use of thermal decomposition for scalable defect engineering and provides a comprehensive relation between crystallographic changes, charge carrier behavior, and band structure modulation. Our findings illustrate that moderate zinc doping (x = 0.03) optimizes the crystal structure and charge carrier mobility, thereby providing a feasible approach for defect-engineered ferrites in optoelectronic and catalytic applications.

2 Materials and methods

2.1 *Material synthesis*

The synthesis of materials involved the use of $Zn(CH_3COO)_2•2H_2O$, $Ni(CH_3COO)_2•4H_2O$, and $FeCl_2•4H_2O$, which were sourced from Sigma-Aldrich and processed using a direct heating method. A mole ratio of 1:2 for Ni to Fe resulted in the production of $NiFe_2O_4$ powders. The prepared mixture was dissolved in 20 mL of deionized water (DI) and agitated for 15 min to ensure uniformity. Additionally, varying proportions of Zn-doped precursors were prepared, followed by calcination at a temperature of 900 °C for 3 h, resulting in the formation of $Zn_xNi_{(1-x)}Fe_2O_4$ formulations corresponding to different Zn concentrations.

2.2 *Characterization*

X-ray diffraction analysis (XRD) (Siemens model D500) using Cu K_α radiation (wavelength of 1.54178 Å) in the 20°–80° range. The morphology and elemental analysis of the synthesized powders were determined by utilizing a scanning electron microscope (SEM) (JEOL model JSM-6335F). The Fourier Transform Infrared Spectrometer (FTIR), Thermo Scientific model Nicolet 6700, was utilized to analyze the structural bonding vibrations within the spectral range of 400 to 4000 cm^{-1}. Additionally, the optical characteristics were evaluated using a UV-Visible spectrophotometer (Jasco model V-503) within the wavelength range of 400 to 800 nm. A photoluminescence spectrometer (PL) (Jasco model FP-8500) with an excitation wavelength of 369 nm was used to study intrinsic defects and exciton recombination. Electrical impedance was measured with an LCR meter and particle-like probes (Keysight Technologies model E4980A/E4980AL), operating at a frequency of 20–2 MHz.

3 Results and Discussion

3.1 *Phase formation, structural properties, and morphology*

The synthesis of $NiFe_2O_4$ from $Ni(CH_3COO)_2•4H_2O$ and $FeCl_2•4H_2O$ encompasses the formation of metal oxides as intermediates at reduced temperatures. Thus, a comprehensive understanding of the decomposition mechanism is necessary to facilitate effective phase development. Previous thermogravimetric analyses have demonstrated that $Ni(CH_3COO)_2•4H_2O$ decomposes into a basic acetate intermediate, represented by the formula $[(1-x)NiAc_2•xNi(OH)_2]$ (Equation (1)) [10]. The study elucidated the decomposition pathways of intermediate compounds of $Ni(OH)_2$, which decomposes to NiO and H_2O within 370–390 °C (Equation (2)).

$$Ni(CH_3COO)_2 • 4H_2O\ (s) \rightarrow\ 0.86Ni(CH_3COO)_2 • 0.14Ni(OH_2)\ (s) + 0.28CH_3COOH(g)\uparrow + 3.72H_2O\ (g)\uparrow \quad (1)$$

$$Ni(OH)_2\ (s) \rightarrow NiO\ (s) + H_2O\ (g)\uparrow \quad (2)$$

The high-temperature hydrolysis of divalent ferric chloride ($FeCl_2•4H_2O$) was heated at 600 °C

under an oxidizing atmosphere. As revealed in Equation (3), a precursor of $FeCl_2$•$4H_2O$ with a mole of 2 gives a final product of Fe_2O_3 [11]. The observed Gibbs energy (ΔG°) is –678.0 kJ / mol, indicating that Fe_2O_3 is a prominent phase.

$$2FeCl_2•4H_2O\ (s) + 0.5O_2\ (g) \uparrow \rightarrow Fe_2O_3\ (s) + 4HCl\ (g) \uparrow + 6H_2O\ (g) \uparrow \quad (3)$$

Owing to the single step of thermal decomposition, $Zn(CH_3COO)_2$•$2H_2O$ was simultaneously heated with other starting materials. The phase transforming to ZnO was reported at 300 °C [12]. According to the study of Chih-Cheng Lin *et al*. [13], the decomposition reaction was described as follows (Equations (4)–(7)).

$$Zn(CH_3COO)_2 • 2H_2O \rightarrow Zn(CH_3COO)_2 + 2H_2O \uparrow \quad (4)$$

$$4Zn(CH_3COO)_2 • 2H_2O \rightarrow Zn_4O(CH_3COO)_6 + 2CH_3COOH \uparrow \quad (5)$$

$$Zn_4O(CH_3COO)_6 + 3H_2O \rightarrow 4ZnO + 6CH_3COOH \uparrow \quad (6)$$

$$Zn_4O(CH_3COO)_6 \rightarrow 4ZnO + 3CH_3COOH_3 \uparrow + 3CO_2 \uparrow \quad (7)$$

After the gaseous phase separation, the remaining solid phases of NiO, Fe_2O_3, and ZnO became a second precursor for the Zn-doped $NiFe_2O_4$ synthesis. The trace amount of ZnO dopant was not detected, suggesting the complete diffusion into the majority phase. Thus, the plausible $NiFe_2O_4$ formation can be expressed as follows (Equation (8)).

$$(1-x)NiO\ (s) + xZnO(s) + Fe_2O_3\ (s) \rightarrow Zn_xNi_{(1-x)}Fe_2O_4\ (s) \quad (8)$$

The determination of the emerging phases of $Zn_xNi_{(1-x)}Fe_2O_4$ samples was facilitated by the presence of an XRD diffractogram, detecting a 2θ ranging from 20° to 80°. As depicted in Figure 1(a)–(d), the diffraction patterns reveal the crystal planes of (200), (311), (222), (400), (422), (511), (440), (620), (533), and (622), which are attributed to the cubic structure of $NiFe_2O_4$ (JCPDS No.074-2081), corresponding with the report of Manikandan *et al*. [14]. Compared to pure $NiFe_2O_4$ (Figure 1(a)), the x = 0.03 sample shows a shift of the (311) peak toward higher angles and broader peaks, indicating lattice distortion caused by Zn^{2+} incorporation and increased defect formation (Figure 1(b)). At the x = 0.05–0.07 samples, peak narrowing is observed, suggesting improved lattice ordering and defect reduction (Figure 1(c)–(d)). By incorporating x= 0.009 (Figure 1(f)), the cubic structure of NiO (JCPDS files No. 75-0197) and the rhombohedral structure of α-Fe_2O_3 (JCPDS files No. 33-0664) were observed as final substances [15], indicating that the incomplete $NiFe_2O_4$ formation causes the high Zn doping effect. The intensity referred to as Fe_2O_3 is more significant than that of the NiO phase, suggesting a greater quantity of Fe_2O_3. Following the report of Ito *et al*. [16], a large amount of Zn addition reduces the oxidation process of Fe^{2+} to Fe^{3+}. Due to the small value of Fe^{2+} observation, the result decreases the phase development from Fe_2O_3 to $NiFe_2O_4$. An insignificant phase fraction of residual NiO results from the reduction of Fe^{3+}, leading to an incomplete reaction.

Table 1 presents the crystallography details, constants, and physical properties of the synthesized materials. The (311) plane's position and FWHM decrease as dopant concentration exceeds 3 at%. The lattice parameter (a) and crystallite size (G) were calculated along Equations (9) and (10), respectively. Given d denotes the spacing between crystal planes, (hkl) represents Miller indices, λ is the Cu K_α X-ray wavelength (λ = 1.54178 Å), β is the FWHM in radians, and θ is the Bragg's angle (degree).

$$a = d \times (h^2 + k^2 + l^2)^{0.5} \quad (9)$$

$$G = \frac{0.9\lambda}{\beta cos\theta} \quad (10)$$

Disorder in atoms is crucial for forming defects and dislocations during crystal growth. The strain (%) was calculated using Equation (11). The value was approximated by comparing the size change to the $NiFe_2O_4$ JCPDS No.74-2081, with a lattice parameter of 8.34 Å and unit cell volume of 579.66 $Å^3$. This term reflects the mechanical behavior and stability of crystalline materials. Structural reliability can be assessed by analyzing strain (ε) and dislocation density (δ), which determine crystal quality. Equations (12) and (13) verify strain and dislocation density, respectively.

$$strain\ (\%) = \frac{(lattice\ parameter_{cal} - lattice\ parameter_{database})}{lattice\ parameter_{database}} * 100 \quad (11)$$

$$\varepsilon = \frac{\beta\ cos\ \theta}{} \quad (12)$$

$$\delta = \frac{1}{G^2}^4 \quad (13)$$

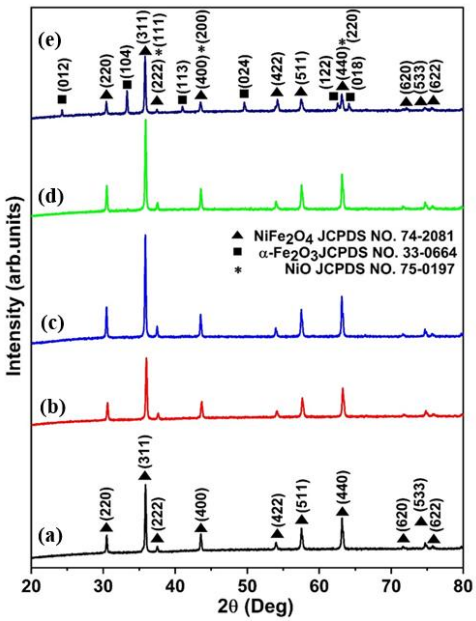

Figure 1: XRD diffractogram of $Zn_xNi_{(1-x)}Fe_2O_4$ for Zn doping concentrations of (a)–(e), assigned to x = 0–0.09, respectively.

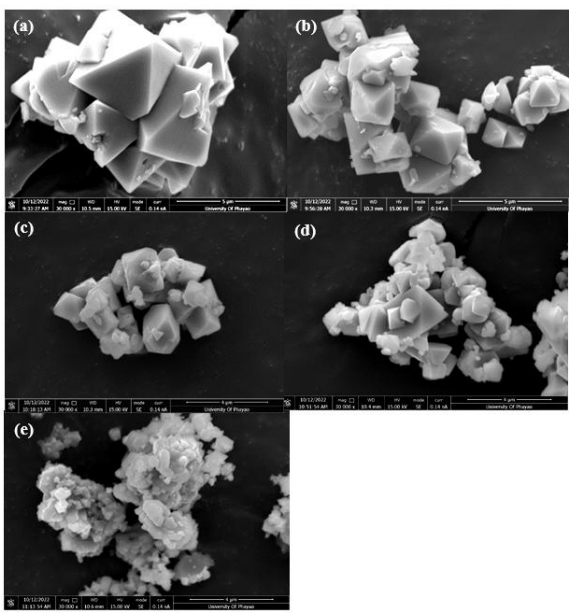

Figure 2: SEM images of $Zn_xNi_{(1-x)}Fe_2O_4$ for Zn doping concentrations of (a)–(e), assigned to x = 0–0.09, respectively.

Increasing the dopant quantity affects the cubic structure's lattice parameter (a). The initial decrease at x=0.03 results from lattice contraction due to Zn^{2+} ions substituting Ni^{2+} ions. When x ≥ 0.05, lattice expansion was found because of defect-induced distortions. Compared to JCPDS No. 74-2081 value of 8.34 Å, x = 0.09 shows the closest value, suggesting the influence of dopant on $NiFe_2O_4$ phase formation during phase development. The trend in crystallite size indicates a decrease at x = 0.03 (94.42 nm), followed by increases at x = 0.05 and x = 0.07. This behavior reflects the balance between reduced grain boundary energy and defect accumulation. At x=0.03, higher dislocation density (11.22×10^{13} lines/m²) and strain confirm lattice distortions that hinder crystal growth. For the $NiFe_2O_4$ phase, x = 0.05 improves crystallinity, corresponding to the highest XRD intensity. This suggests that moderate Zn doping optimizes lattice ordering, reduces strain, and enhances crystal quality. The unit cell volume correlates directly with the lattice parameter. As x = 0–0.09, the unit cell volumes were 571.99, 564.42, 573.66, 571.61, and 575.07 Å³, differing from JCPDS No. 74-2081 (579.66 Å³). The unit cell contracts at x = 0.03 and expands at x = 0.05, consistent with defect-related strain behavior. A percentage strain reduction beyond x = 0.03 implies that defects are stabilized or redistributed, thereby reducing dislocation density and improving crystallinity. The strain, as calculated using Equation (14), exhibits a trend similar to the percentage strains, confirming significant atomic displacement at x = 0.03. Calculated dislocation density shows peaks at x = 0.03, with a decrease in dislocation observed as the dopant concentration exceeds 3 at%. Low crystallinity is observed at x = 0.03, whereas doping with x = 0.05–0.07 reveals a superior crystal arrangement, as indicated by the XRD intensity in Figure 2(c)–(d).

The X-ray density (ρ_x) as a function of lattice parameter (a) has been calculated according to the following relation [17].

$$\rho_x = \frac{ZM}{N_A a^3} \quad (14)$$

Where Z refers to the number of formula units in the unit cell (Z = 8), N_A variable represents an Avogadro's number ($6.02 * 10^{23}$ mol^{-1}), and M is the molecular weight (234.38 g mol^{-1} for $NiFe_2O_4$ structure). As presented in Table 1, the X-ray density values of $Zn_xNi_{(1-x)}Fe_2O_4$ reveal a converse trend with the lattice parameter quantity. The X-ray density of x = 0–0.09 is 5.45, 5.52, 5.43, 5.45, and 5.42 g/cm³, corresponding to the previous report of $NiFe_2O_4$ (5.44 g/cm³) [18]. The decreasing density with increasing Zn content can be attributed to the ionic radii of the components and the change in atomic weight.

Table 1: The structural constants, defects, and bonding distance of the as-synthesized samples.

$Zn_xNi_{(1-x)}Fe_2O_4$	x = 0	x = 0.03	x = 0.05	x = 0.07	x = 0.09
(311) crystal plane position (2θ)	35.88	36.04	35.84	35.89	35.81
FWHM (2θ)	0.12	0.18	0.13	0.13	0.06
Lattice parameter (Å)	8.30	8.26	8.31	8.30	8.32
Unit cell volume $(Å)^3$	571.99	564.42	573.66	571.61	575.07
Crystallite size (nm)	141.52	94.42	130.66	130.68	283.22
Strain (%)	0.443	0.884	0.346	0.465	0.265
Strain $*10^{-4}$	2.451	3.674	2.655	2.655	1.225
Dislocation density $*10^{13}$ (lines/m^2)	4.99	11.22	5.86	5.86	1.25
X-ray density (g/cm^3)	5.45	5.52	5.43	5.45	5.42
Hydrodynamic diameter (μm)	95.22 ±37.78	39.24 ±5.70	44.49 ±8.42	65.15 ±17.62	40.70 ±50.35
Specific surface area $*10^{-2}$ (m^2/g)	1.16	2.77	2.48	1.69	2.72
Hopping length at A-site (d_A) (Å)	3.594	3.579	3.598	3.594	3.600
Hopping length at B-site (d_B) (Å)	2.935	2.922	2.938	2.934	2.940
Cation-anion distances at A-site (d_{AL}) (Å)	1.885	1.887	1.887	1.885	1.888
Cation-anion distances at B-site (d_{BL}) (Å)	2.026	2.017	2.028	2.025	2.030

Table 2: The atomic coordinates and statistical parameters of the as-synthesized samples calculated by Rietveld refinement.

Samples $Zn_xNi_{(1-x)}Fe_2O_4$		**x = 0**	**x = 0.03**	**x = 0.05**	**x = 0.07**		**x = 0.09**	
Phase (wt%)		$NiFe_2O_4$ (100%)	$NiFe_2O_4$ (100%)	$NiFe_2O_4$ (100%)	$NiFe_2O_4$ (100%)	Fe_2O_3 (5.50%)	NiO (4.55%)	$NiFe_2O_4$ (89.95%)
Atomic coordinates		**Ni**	**Ni**	**Ni**	**Ni**	-	**Ni**	**Ni**
	x	0	0	0	0		0	0
	y	0	0	0	0		0	0
	z	0	0	0	0		0	0
		Fe	**Fe**	**Fe**	**Fe**	**Fe**	-	**Fe**
	x	0.6250	0.6250	0.6250	0.6250	0		0.62500
	y	0.6250	0.6250	0.6250	0.6250	0		0.62500
	z	0.6250	0.6250	0.6250	0.6250	0.3553		0.62500
		O	**O**	**O**	**O**	**O**	**O**	**O**
	X	0.6250	0.6250	0.2429	0.2445	0.3056	0.5000	0.2425
	Y	0.6250	0.6250	0.2429	0.2445	0	0.5000	0.2425
	z	0.6250	0.6250	0.2429	0.2445	0.2500	0.5000	0.2425
R's	**Sig (%)**	9.14	11.26	14.87	16.03		15.95	
	R_{exp} (%)	0.76	0.73	0.71	0.70		0.69	

In the spinel lattice, the distance between the magnetic cations at the tetrahedral and octahedral sites, represented by the Hopping length at the A site (d_A) and B site (d_B), respectively, can be represented as a function of the lattice parameter (a). This distance can be calculated using Equations (15)–(16) [3].

$$d_A = 0.25a\sqrt{3} \quad (15)$$

$$d_B = 0.25a\sqrt{2} \quad (16)$$

By using the oxygen parameter (u), the cation-anion distances at the A-site (d_{AL}) and B-site (d_{BL}) can be determined by following relations (Equations (17)–(18)) [19]. The oxygen parameter value for the $NiFe_2O_4$ structure was 0.38 [20].

$$d_{AL} = a\sqrt{3}\ (u - 0.25) \quad (17)$$

$$d_{BL} = a(3u^2 - \frac{11}{4}u + \frac{43}{64})^{0.5} \quad (18)$$

Dopants with x = 0–0.09 produced varying hopping lengths at the tetrahedral site (d_A) (3.594, 3.579, 3.598, 3.594, and 3.600 Å) and the octahedral site (d_B) (2.935, 2.922, 2.938, 2.934, and 2.940Å), as shown in Table 1. The octahedral site has shorter hopping lengths than the tetrahedral site, indicating a higher probability of electron hopping between cations at the B-site than at the A-site [21]. This leads to differences in electrical and magnetic characteristics between the two sites [22]. The cation-anion distance trends mirror the hopping length: with increased doping, the distances are 1.885, 1.887, 1.887, 1.885, and 1.888 Å for the A-site, and 2.026, 2.017, 2.028, 2.025, and 2.030 Å for the B-site.

The changes in lattice parameters and unit cell volume of $Zn_xNi_{(1-x)}Fe_2O_4$ are crystallographically explained by differing cation sizes. $NiFe_2O_4$ has a face-centered cubic (FCC) structure with cations in tetrahedral (A) and octahedral (B) positions.

Replacing Ni^{2+} (0.69 Å) with larger Zn^{2+} ions (0.74 Å) [23] causes lattice distortions and expansion of the unit cell. Initially, the lattice parameter decreases for $x \leq 0.03$, then increases for $x \geq 0.05$, reflecting the complex interactions between distortions and cation rearrangements.

X-ray diffraction (XRD) data were systematically evaluated for their structural characteristics utilizing the Rietveld refinement method [24]. This analysis was conducted using the MAUD software package [25], which processed the Crystallographic Information File (CIF) acquired from the Crystallography Open Database (COD). The CIF numbers 9015964, 4320490, and 5910064 correspond to Fe_2O_3, NiO, and $NiFe_2O_4$ structures. Zn doping (x = 0–0.09) affected structural constants by changing atomic positions, generating defect sites. Additionally, doping led to an increase in dislocation density and strain by affecting neighboring atoms, thus confirming that doping results in modifications and distortions within the crystals.

Statistical parameters for the Rietveld experiment (R_{exp}) and goodness of fit (Sig) show a satisfactory fit, with both values below 10%, indicating reliable refinement [26]. For a higher Sig value, high-precision data were included to extend the description beyond the insignificant atomic arrangement [27]. As shown in Table 2, the coordination of oxygen atoms in the $NiFe_2O_4$ structure sharply decreases as $x > 0.03$, indicating an interstitial or replaced atom. This study demonstrates a greater goodness of fit with doping levels of x = 0.07 and 0.09, confirming a greater disturbance in the host lattice.

Figure 2 shows SEM images of $Zn_xNi_{(1-x)}Fe_2O_4$ samples, revealing octahedral particles with a broad size distribution at Zn additions below 9 at%. At x = 0.09, agglomerated irregular particles appear (Figure 2 (f)), attributed to incomplete processes rather than the breaking of $NiFe_2O_4$. Average lengths are 2.69 ± 1.03, 1.74 ± 0.48, 1.18 ± 0.31, 1.24 ± 0.48, and 0.93 ± 0.43 m for x = 0 - 0.09. This morphology indicates decreased size with increasing Zn concentration, confirming dopant disturbance in crystal growth and hindering formation due to crystal imperfections.

The octahedral structure forms via a dissolution-recrystallization mechanism [28]. This crystal growth is influenced by reduced viscosity and acidity, which enhances atomic diffusion and promotes rapid growth along the (100) and (111) directions [29]. The octahedron has 8 stable facets with low surface energy due to the rapid development of crystallographic planes [30].

Zn doping at x = 0.03 causes lattice strain and increases dislocation density but preserves phase purity. Better crystallinity and defect formation are essential for electronic tuning. Additionally, the thermal decomposition method offers crystallographic control. Interestingly, Zn-doped $NiFe_2O_4$ promises a defect-engineered platform for optoelectronic applications.

An energy-dispersive X-ray (EDX) analysis was used to determine the atomic composition of the synthesized products. At x = 0, the Ni:Fe:O atomic ratio is 1:2.45:2.60, indicating oxygen deficiency. Incorporating Zn by replacing Ni atoms at 3-9 at% shows a lower observed quantity of dopants at 0.17, 1.32, 1.51, and 2.90 at%, respectively. Manipulating added atoms through solid-state synthesis appears to be challenging. For doped conditions, the atomic ratios (Zn+Ni: Fe: O) for x = 0.03, 0.05, 0.07, and 0.09 are 1:2.15:3.49, 1:2.55:1.88, 1:2.53:1.79, and 1:2.23:6.84, respectively. This finding highlights the impact of the Zn dopant on the host lattice. The atomic ratio for x = 0.03 is closest to the regular $NiFe_2O_4$ structure. The oxygen fraction is adequately increased compared to other conditions. The x = 0.09 condition exhibits an excessive oxygen content (6.84 at%), resulting in prominent defect sites, phase transition, and altered crystallinity and crystallite sizes.

As depicted in Figure 3, the size distribution of the as-produced particles was assessed using the Dynamic Light Scattering (DLS) method. The estimation of particle size is calculated using the Stokes-Einstein equation (Equation (19)). The terms of D_H, f, k_B, η, and D denote the particles' hydrodynamic diameter, friction coefficient, Boltzmann constant, solvent viscosity, and diffusion coefficient, respectively [31].

$$D_H = \frac{k_B T}{f} = \frac{k_B T}{3\pi\eta D} \quad (19)$$

The distribution method illustrates particle sizes, providing an average size (mean) and span for each peak in the particle size distribution histogram (PSD). The mean particle size of $Zn_xNi_{(1-x)}Fe_2O_4$ for x = 0, 0.03, 0.05, 0.07, and 0.09 is 95.22 ± 37.78 µm, 39.24 ± 5.70 µm, 44.49 ± 8.42 µm, 65.15 ± 17.62 µm, and 40.70 ± 50.35µm. Trends in crystallite values and hydrodynamic diameter of particles are similar, supporting the influence of dopant concentration on bond strength and surface charge, which affects

crystallite size and particle agglomeration. The approximated particle size exceeds expectations, potentially leading to agglomeration due to high-temperature calcination, Van der Waals forces, and magnetic interactions [31].

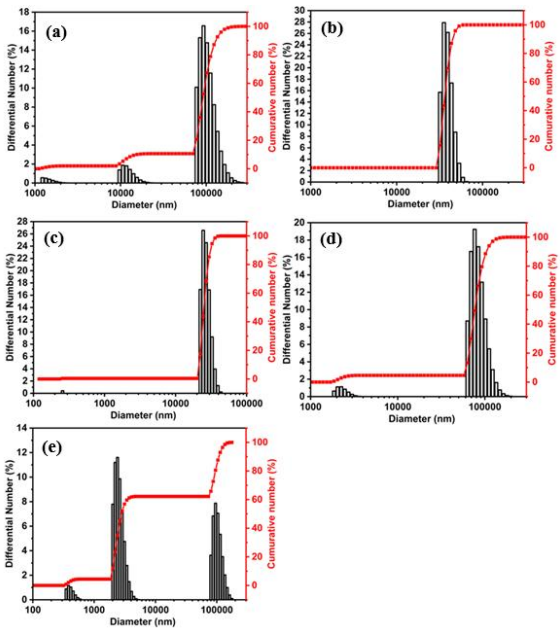

Figure 3: The particle size using the dynamic light scattering method of $Zn_xNi_{(1-x)}Fe_2O_4$ for Zn doping concentrations of (a)–(e), assigned to x = 0–0.09, respectively

DLS analysis estimated the average particle size to assess surface area. The specific surface area (SSA) is surface area per unit mass or volume, calculated using the following Equation (20) [32].

$$SSA = \frac{6000}{\rho_x D_H} \quad (20)$$

The values of X-ray density (ρ_x) and hydrodynamic diameter (D_H) were taken to determine the SSA quantity. The estimated SSA values ($*10^{-2}$) of $Zn_xNi_{(1-x)}Fe_2O_4$ were 11.57, 27.71, 24.84, 16.90, and 27.22 m^2/g when x was shown to be 0, 0.03, 0.05, 0.07, and 0.09. At x = 0.09, the most significant area was identified, attributed to the formation of the $NiO\text{-}Fe_2O_3\text{-}NiFe_2O_4$ composite. Comparing the conditions prepared for the pure $NiFe_2O_4$ phase, x = 0.03 significantly presents the highest SSA value. The value is less significant than that of the co-precipitation process - $NiFe_2O_4$, which shows an SSA value of 52.1 m^2/g [9]. It should be noted that the SSA inversely relates to the density and particle size.

In summary, the DLS results show a significant decrease in particle size with more Zn, with x = 0.03 giving the most uniform and compact distribution. These trends match the crystallite size variations seen in XRD, confirming that Zn doping impacts microstructure and surface properties.

The sample with x = 0.09 will not be further studied due to the presence of NiO, Fe_2O_3, and $NiFe_2O_4$ phases. Emphasizing the Zn effect on $NiFe_2O_4$ structure, the samples with a pure phase of $NiFe_2O_4$ were determined to have modified structures and characteristics.

The FT-IR analysis determined the chemical functional groups of $NiFe_2O_4$ (with Zn at x = 0–0.07) in the 400 to 2,500 cm^{-1} range, as shown in Figure 4(a). All samples showed minority peaks at 2,350 cm^{-1} due to C-N bonding vibrations [33], indicating residual precursors. A small shoulder peak around 630 cm^{-1} represented Ni–O or Fe–O stretching in tetrahedrally coordinated metal ions [34]. Vibrations between the tetrahedral cation (A-site) and oxygen were noted at 550 cm^{-1} and 590 cm^{-1}, indicating Fe^{3+}-O (trivalent cations, T_d-site) and Ni^{2+}-O (divalent cations, O_h-site) vibrations [35]. Due to low signal intensity, signals below 500 cm^{-1} were unclear for spectral analysis. The spectral vibration around 415–425 cm^{-1} indicates the presence of the octahedral metal complex [36].

Considering the magnification figures, the spectrum for vibrations in tetrahedral and octahedral cation sites is shown in Figures 4(b) and (c). The spectral peaks at 538 and 580 cm^{-1} shifted due to the change in the coordination of Fe ions from octahedral to tetrahedral structures [19]. The spectra at approximately 586 and 547 cm^{-1} show negligible wavenumber changes, indicating insignificant Fe movement. However, the decreasing intensities in this range also suggest cation movement from octahedral to tetrahedral structures [28]. This aligns with the shorter hopping distance within octahedral locations, allowing easier movement of charge carriers compared to tetrahedral sites. Tetrahedral metal complexes show higher wavenumbers than octahedral complexes, reflecting reduced cation-oxygen bond lengths. The shorter bond length requires more vibration energy, resulting in longitudinal vibrations along the cation-oxygen axis in tetrahedral sites and transverse vibrations in octahedral sites. This prominent peak demonstrates stronger intensity under x=0.05 and 0.07 doping conditions, indicating better crystallinity than other samples.

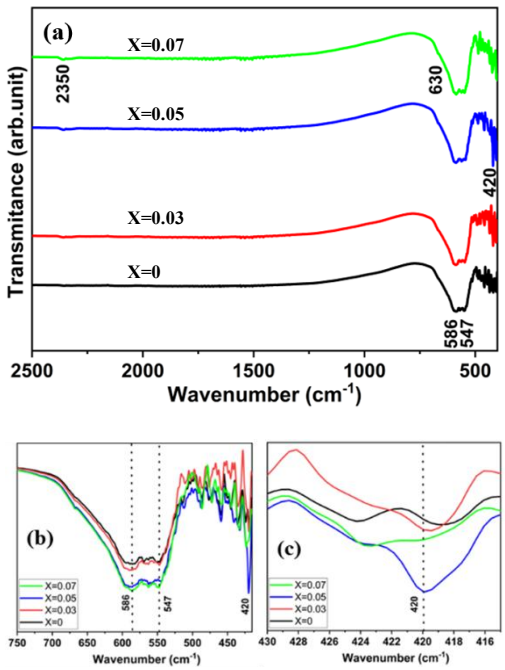

Figure 4: FT-IR spectra of $Zn_xNi_{(1-x)}Fe_2O_4$ with the wavenumber range of (a) 400 - 2500 cm^{-1}, (b) 410–750 cm^{-1}, and (c) 414–430 cm^{-1}.

Table 3: FT-IR vibration frequency and force constant of octahedral and tetrahedral sites.

Samples	x = 0	x = 0.03	x = 0.05	x = 0.07
ν_T (cm^{-1})	547.0	547.3	544.0	547.4
F_T (*10^{-2} Nm^{-1})	2.178	2.181	2.155	2.182
ν_O (cm^{-1})	418.0	419.5	420.0	421.0
F_O (*10^{-2} Nm^{-1})	1.272	1.281	1.284	1.290

The force constant directly impacts the correlation between the metal and oxygen ion bond length and the frequency change in the absorption band. Additionally, the force constants for tetrahedral (F_T) and octahedral (F_O) positions were calculated using the following relation, as shown in Equation (21) [37].

$$F = 4\pi^2 * c^2 * \nu^2 * \mu \quad (21)$$

Where F is the force constant, c is the speed of light ($2.99*10^8$ ms^{-1}), ν denotes the vibration frequency for tetrahedral (ν_T) and octahedral (ν_O) positions, and μ signifies the reduced mass of Fe^{3+} and O^{2-} ions (about $2.065*10^{-26}$ kg mol^{-1}). As shown in Table 3, the estimated force constants (*10^{-2} Nm^{-1}) for samples with x = 0, 0.03, 0.05, and 0.07 were 2.178, 2.181, 2.155, and 2.182 for tetrahedral positions (F_T), and 1.272, 1.281, 1.284, and 1.290 for octahedral positions (F_O). The replacement of Ni^{2+} by Zn^{2+} influences the force constant in A and B sites due to cation redistribution [38]. The force constants increase with Zn concentration. Variations in cation-oxygen bond length explain this trend. Increasing the number of zinc dopants decreases the bond length, thereby increasing the energy required to break the shorter bonds. Additionally, the exchange of Fe^{3+} and Ni^{2+} ions between octahedral and tetrahedral sites in the structures is influenced by the force constant and the grain size [39]. These factors contribute to the higher force constant of tetrahedral sites.

The FT-IR spectra confirm metal–oxygen bonding in both tetrahedral and octahedral sites, with shifts in vibration frequency and force constants indicating cation redistribution caused by Zn doping. These subtle alterations support the structural adjustments observed in XRD and strengthen the defect-driven modifications within the spinel lattice.

3.2 *Optical properties and impedance measurements*

The energy bandgap (Eg) of the semiconductor can be derived from the absorption spectra, which are characterized by the relationship between the absorption coefficient (α) and photonic energy (hν). This is expressed by the Wood and Tauc equation, as shown in Equation (22) [40].

$$\alpha h\nu = (h\nu - Eg)^n \quad (22)$$

The variables of h, ν, and Eg represent the Planck constant, photon frequency, and photonic energy bandgap, where n is an integer for the direct energy bandgap (n=1/2). Figure 5 shows plots of photon energy versus $\alpha h\nu^2$. The Eg value is estimated by extending the linear portion at $\alpha h\nu^2 = 0$. Direct transition Eg values are 1.62, 1.52, 1.45, and 1.43 eV for samples with x = 0, 0.03, 0.05, and 0.07, respectively. The pristine $NiFe_2O_4$ has a similar Eg value of 1.67 eV [28]. The Eg values reflect electron movement from the valence band (VB) of the O-2p energy level to the conduction band (CB) of the 3-d (t2g-eg) energy level [41]. The crucial factors affecting the direct transition Eg are crystallite size, crystal disorder, and impurities [3]. The XRD study shows changes in lattice parameter, crystallite size, and defect density due to host lattice and dopant interaction (Table 1). The reduction in transition Eg

results from electron exchange between delocalized conduction bands and localized d-shell electrons of Zn^{2+} ions. Replacing Ni^{2+} ions with dopant ions increases the valence band potential and decreases the conduction band potential, leading to reduced Eg [42].

The UV–V is absorption analysis shows bandgap narrowing with increased Zn, reaching a minimum at x = 0.07. This redshift relates to larger crystallite size, fewer defects, and better structural order in XRD data. Zn doping enhances visible-light absorption, benefiting optoelectronic and photocatalytic applications.

Further analysis following an Eg determination, the edge potentials of the valence band (E_{VB}) and conduction band (E_{CB}) can be understood by Mulliken electronegativity theory, as presented in Equations (23) and (24).

$$E_{VB} = X\text{-}Ee + 0.5Eg \quad (23)$$

$$E_{CB} = E_{VB} - Eg \quad (24)$$

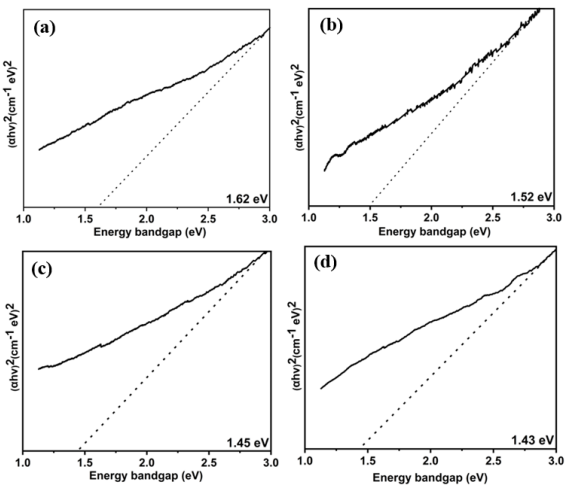

Figure 5: Direct energy bandgap of $Zn_xNi_{(1-x)}Fe_2O_4$ for Zn doping concentrations of (a)–(d), assigned to x = 0–0.07, respectively

The variable X represents Mulliken's absolute electronegativity, which is 4.69 eV for $NiFe_2O_4$. The free electrons' energy (Ee) was reported for the ~4.5 eV SHE [43]. As dopant concentration up to X=0-0.07, the calculated quantities were revealed to be -0.620, -0.570, -0.535, and -0.525 eV for E_{CB} and 1.000, 0.950, 0.915, and 0.905 eV for E_{VB}, as demonstrated in Table 4. The edge potential and energy bandgap of $Zn_xNi_{(1-x)}Fe_2O_4$ are depicted in Figure 6.

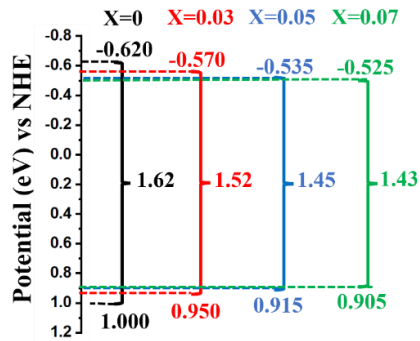

Figure 6: The edge potential and energy bandgap of $Zn_xNi_{(1-x)}Fe_2O_4$ when x = 0–0.07.

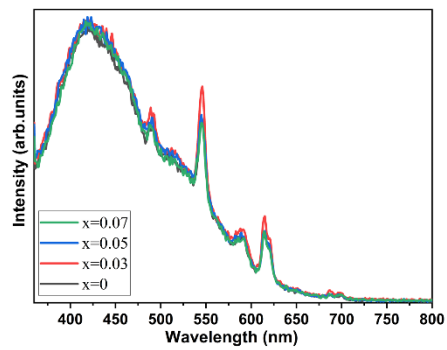

Figure 7: The PL emission of $Zn_xNi_{(1-x)}Fe_2O_4$ when x = 0–0.07.

Photoluminescence spectroscopy (PL) was employed to analyze the charge carriers and the appearance of imperfections in semiconductors by studying exciton emissions. The PL emission spectra of the initial samples were observed in the visible region. As illustrated in Figure 7, the PL emission spectra of the samples were shown in the range of 325 to 800 nm.

Table 4: The quantity of direct Eg, conduction band, and valence band potentials of $Zn_xNi_{(1-x)}Fe_2O_4$.

Samples	Direct Energy Bandgap (eV)	Conduction Band (E_{CB}) (eV)	Valence Band (E_{VB}) (eV)
x = 0	1.62	-0.620	1.000
x = 0.03	1.52	-0.570	0.950
x = 0.05	1.45	-0.535	0.915
x = 0.07	1.43	-0.525	0.905

The emission spectrum varied in signal intensity, associated with crystallinity, defective surface, and organic residual [44]. The presence of defects, representing low crystallinity, and organic

residual materials, acts as charge trappers. Luminescence quenching primarily occurs due to reduced charge transfer. All samples showed PL spectra with a comparable pattern. As observed, the signal intensity of the x = 0.03 condition is superior to that of the other samples. The finding indicates the formation of the highest crystallinity, leading to more accessible electron-hole recombination.

This study found the strongest peak at around 410–430 nm with a broad spectral range of 360–475 nm. The oxygen vacancies in the $NiFe_2O_4$ lattice were found at the emission peak of 410 nm [45]. The transition of 3T1g (3P) ← 3A2g (3F), observed at 415 nm, can be assigned to the trapped electron traveling from the Ni interstitial sites to the valence band [28] and Ni^{2+} occupying the O sites in the hexagonal structures [44]. According to the previous report, the emitted spectrum at 420 nm was generated due to the polaronic effect, which increased interactions between electrons and phonons. The spectrum at 490 nm refers to the 3T2g (3F) ← 3A2g(3F) transition, which is attributed to Ni^{2+} cations at the O_h-sites in the $NiFe_2O_4$ structures [44]. The spectrum at around 545 nm was assigned to the transition of Fe^{3+} ions, as described in the relation of the 3d34s ←3d5 [46]. The sample of x = 0.03 reveals that the strongest intensity corresponds to the shortest hopping length and cation-anion distance, as exhibited in Table 1. At the emission of 593 nm, the peak corresponds to the 3T1 (3P) ← 3T1 (3F) transition that reflects the Fe^{3+} cations at the T_d-site of the $NiFe_2O_4$ lattice [44]. The orange emission at 610 nm corresponds to the oxygen vacancies [44]. Naik *et al*., reported that Ni^{2+} ions appear at both T_d-site and O_h-site, resulting in the emission in the orange-red and violet-blue regions, respectively [44]. The difference in emission intensity from the blue to the orange band may cause the shared site of 2 divalent cations (Zn^{2+} and Ni^{2+}) to change the e^-- h^+ recombination.

The enhanced PL at x = 0.03 aligns with reduced defect density and shorter hopping distances, indicating more efficient electron–hole recombination. These results validate the structural-optical coupling enabled by moderate Zn doping.

An LCR meter was used to measure the impedance. As a result of the Nyquist plots in Figure 8, the impedance spectroscopy exhibits a signal with a semi-circle shape. The signal describes the specific mechanisms, including charge transfer and resistance at grain boundaries and within the grains [47]. The relaxation time associated with the resistance at grain boundaries and the interior of grains can be represented through the Cole-Cole Equation (25) [48].

$$Z = Z' + Z''j = R_G + \frac{R_{GB}}{1+(j\omega_m R_{GB} C)^{(1-\alpha)}} \quad (25)$$

Where $Z'$and Z'' are assigned to be the real part and the imaginary part of the impedance (Z). R_G, R_{GB}, ω_m, C, and α represent the grain interior resistance, the grain boundaries resistance, the frequency at the peak of the semicircle, the capacitance at the grain boundary, and the depression angle. Following previous literature [48], the relaxation time (τ) is calculated along a relation of $\tau = 1/\omega_m$. The resistance at the intersection of the semicircle with the X-axis can be attributed to R_G (lower Z') and $R_G + R_{GB}$ (higher Z'). The semicircle observed in Nyquist plots indicates a dominant grain boundary contribution to resistance, while the smaller arc radius at x=0.03 reflects enhanced charge transport properties. The geometric fit in a semicircle shape without an electronic circuit model was carried out using the Z-view 4 program. The fitting exhibits the higher intersection between the semicircle and the x-axis (interpreted as $R_G + R_{GB}$), ω_m, estimated resistance, estimated capacitance, and the depression angle, demonstrated in Figure 9 and detailed in Table 5. The observed reduction in total resistance at x = 0.03 can be attributed to improved crystallinity, reduced defect density, and enhanced grain boundary conductivity, as confirmed by XRD and SEM analysis.

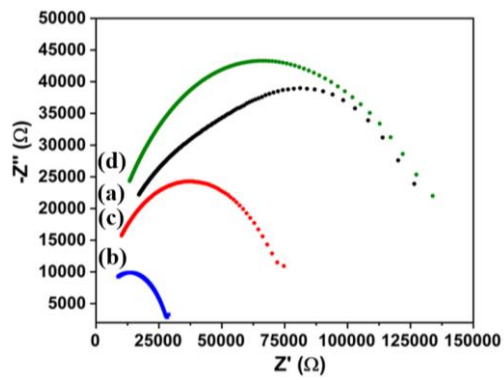

Figure 8: Nyquist plots of $Zn_xNi_{(1-x)}Fe_2O_4$ for Zn doping concentrations of (a)–(d), assigned to x = 0-0.07, respectively.

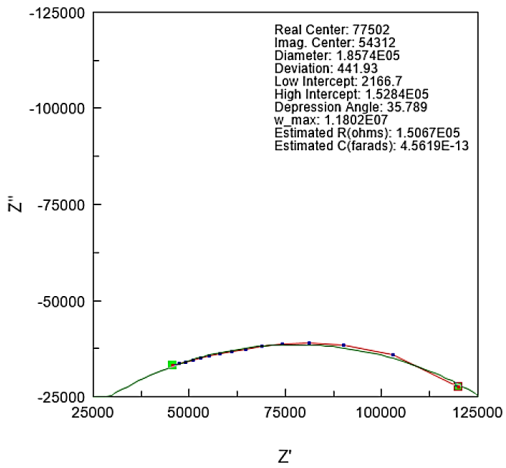

Figure 9: The semicircle fitting and geometric analysis of $Zn_xNi_{(1-x)}Fe_2O_4$ as x = 0.

As observed quantities, the x = 0.03 sample reveals the lowest resistance compared to the other samples, while also exhibiting the most significant relaxation time and capacitance. Due to the proper dopant amount, a favorable distribution of Ni^{2+} and Zn^{2+} ions influences the lattice structure by reducing hopping length and cation-anion distances. This structural optimization reduces charge trapping at grain boundaries, enhancing the material's conductivity and charge storage capacity. This suggests that Zn doping at x = 0.03 effectively enhances charge carrier mobility and storage capacity. The larger capacitance, prolonged relaxation duration, and insignificant resistance in the x = 0.03 sample indicate a complex interaction between charge storage and conduction processes. The increased ability to accumulate electrical charge is associated with the largest surface area, introducing more active sites and grain boundaries. A longer relaxation time indicates that charge carriers can move through the material with fewer disturbances. The mobility (μ) of charge carriers is directly related to the relaxation time. A longer relaxation time allows for higher mobility of charge carriers, resulting in lower resistance. In agreement with the calculated hopping length and cation-anion distance of both A- and B-sites, the shortest values, as found in the x = 0.03, reflect the more effortless movement of charge carriers.

The impedance results confirm that x = 0.03 offers the most favorable charge transport characteristics, as reflected in lower resistance and longer relaxation times. These improvements are closely linked to structural optimization, reduced hopping length, and increased surface activity.

Table 5: A geometric analysis of the semi-circle shape of $Zn_xNi_{(1-x)}Fe_2O_4$.

Samples	ω_m *10^7 (rad/s)	τ *10^{-7} (s)	R *10^5 (Ω)	C *10^{-13} (F)	α (θ)
x = 0	1.180	0.847	1.507	4.562	35.79
x = 0.03	7.043	1.042	0.378	31.804	32.18
x = 0.05	1.034	0.967	0.905	8.918	33.45
x = 0.07	1.185	0.844	5.479	1.138	42.36

4 Conclusions

$Zn_xNi_{(1-x)}Fe_2O_4$ samples were successfully synthesized via a thermal decomposition process at 900 °C for 3 h, with doping concentrations ranging from x = 0 to 0.09. XRD and Rietveld refinement confirmed the formation of a pure $NiFe_2O_4$ spinel phase up to x = 0.07, while x = 0.09 led to the appearance of secondary phases (Fe_2O_3 and NiO) due to lattice instability. Optimal doping at x = 0.03 led to improved crystallinity, reduced defect density, and minimized cation-anion distances. SEM and DLS analyses showed that Zn doping decreased particle size and affected octahedral morphology. Optical characterization revealed a progressive reduction in bandgap energy from 1.62 eV to 1.43 eV, enhancing visible-light absorption. The strongest photoluminescence emission at the x = 0.03 sample indicates efficient radiative recombination. Electrical impedance analysis confirms enhanced charge transport at x = 0.03, with lower resistance, higher capacitance, and extended relaxation time. All results correlated with minimized hopping length and cation–anion distances. These findings confirm that moderate Zn doping at x = 0.03 effectively modifies the crystallographic structure and charge carrier behavior, resulting in $Zn_xNi_{(1-x)}Fe_2O_4$, a promising option for optoelectronic and photocatalytic applications. Nevertheless, this study is limited to static optical and electrical analyses. Future work will explore magnetic behavior, stability, and device integration. Achieving precise dopant control at higher Zn levels remains a key challenge.

Acknowledgments

The authors thank the Unit of Excellence in Advanced Nanomaterials, the School of Science, University of Phayao, for support. This study was funded by the School of Science (Grant No. PBTSC67002) and supported by the Thailand Science Research and Innovation Fund via the University of Phayao.

Author Contributions

A. K.: contributed to the study's conception and design. All authors conduct experiments; W.J., S.K., and P.S.: examined optical and electrical characteristics; P.R., A.P., and A.K. performed the analysis and interpretation of data; P.R. and A.K. drafted the manuscript, which A.K. revised for important intellectual content. All authors approved the final manuscript.

Conflicts of Interest

The authors declare no conflict of interest.

References

[1] N. Vasoya et al., "Synthesis of nanostructured material by mechanical milling and study on structural property modifications in $Ni_{0.5}Zn_{0.5}Fe_2O_4$," *Ceramics International*, vol. 36, no. 3, pp. 947–954, 2010.

[2] K. Mohit et al., "Structural, optical and dielectric studies of $Ni_xZn_{1-x}Fe_2O_4$ prepared by auto combustion route," *Physica B: Condensed Matter*, vol. 407, no. 6, pp 935–942, 2012.

[3] W. E. Pottker et al., "Influence of order-disorder effects on the magnetic and optical properties of $NiFe_2O_4$ nanoparticles," *Ceramics International*, vol. 44, no. 14, pp 17290–17297, 2018.

[4] V. A. Samson, "One pot hydrothermal synthesis and characterization of $NiFe_2O_4$ nanoparticles," *Materials Today: Proceedings*, vol. 50, pp. 2665–2667, 2022.

[5] S. Shariati, E. Seyedjafari, F. S. Mahdavi, A. Maali, and E. Ferdosi-Shahandashti, "$NiFe_2O_4$/ZnO-coated Poly (L-Lactide) nanofibrous scaffold enhances osteogenic differentiation of human mesenchymal stem cells," *Frontiers in bioengineering and biotechnology*, vol. 10, p. 1005028, 2022.

[6] Y. Keereeta, "Structural characteristics and visible-light-driven photocatalytic of ZnO@ octahedral $NiFe_2O_4$ microcrystal prepared via thermal decomposition process," *Zeitschrift für Physikalische Chemie*, vol. 237, no. 10, pp. 1457–1482, 2023.

[7] N. Kottam et al., "Design and development of g-C_3N_4/ZnO/CdS ternary photocatalyst for the removal of environmentally hazardous organic dyes under visible light," *Applied Science and Engineering Progress*, vol. 18, no. 2, 2025, Art. no. 7654, doi: 10.14416/j.asep.2024.11.008.

[8] T. Dippong, O. Cadar, and E. A. Levei, "Effect of transition metal doping on the structural, morphological, and magnetic properties of $NiFe_2O_4$," *Materials*, vol. 15, no. 9, p. 2996, 2022.

[9] K. Chatterjee et al., "Exploring the impact of Ni doping in tuning the bandgap, electronic, optoelectronic and photocatalytic properties of $ZnFe_2O_4$," *ChemNanoMat*, vol. 10, no. 11, 2024, Art. no. e202400348.

[10] J. Doremieux, "Thermal evolution of nickel acetate. I. Thermolysis in a nitrogen stream," *Bulletin de la Société Chimique de France*, vol. 1969, no. 5, p. 1508, 1969.

[11] I. Motovilov, "Oxide powders production from iron chloride," *CIS Iron and Steel Review*, vol. 15, pp. 28–32, 2018.

[12] P. Katekaew, "Role of the thermal regime in the defect formation of zinc oxide nanostructures prepared by the thermal decomposition process," *Zeitschrift für Physikalische Chemie*, vol. 237, no. 8, pp. 1077–1104, 2023.

[13] C.-C. Lin and Y.-Y. Li, "Synthesis of ZnO nanowires by thermal decomposition of zinc acetate dihydrate," *Materials Chemistry and Physics*, vol. 113, no. 1, pp. 334–337, 2009.

[14] V. Manikandan, "Structural, dielectric and enhanced soft magnetic properties of lithium (Li) substituted nickel ferrite ($NiFe_2O_4$) nanoparticles," *Journal of Magnetism and Magnetic Materials*, vol. 465, pp. 634–639, 2018.

[15] Y.-L. Kuo, "Assessment of redox behavior of nickel ferrite as oxygen carriers for chemical looping process," *Ceramics international*, vol. 39, no. 5, pp. 5459–5465, 2013.

[16] H. Ito, "Wet chemical synthesis of zinc-iron oxide nanocomposite," *Hyperfine Interactions*, vol. 238, no. 1, p. 79, 2017.

[17] S. Patange, "Rietveld structure refinement, cation distribution and magnetic properties of Al^{3+} substituted $NiFe_2O_4$ nanoparticles," *Journal of Applied Physics*, vol. 109, no. 5, 2011.

[18] G. Umapathy, "Structural, dielectric and AC conductivity studies of Zn substituted nickel ferrites prepared by combustion technique," *Journal of Materials Science: Materials in Electronics*, vol. 27, pp. 7062–7072, 2016.

[19] T. Poudel, "The effect of gadolinium substitution in inverse spinel nickel ferrite: Structural, Magnetic, and Mössbauer study," *Journal of Alloys and Compounds*, vol. 802, pp. 609–619, 2019.

[20] I. A. Campbell, A. Fert, and E. P. Wohlfarth, *Ferromagnetic materials*. Amsterdam: North Holland, 1982.

[21] S. K. Paswan, "Optimization of structure-property relationships in nickel ferrite nanoparticles annealed at different temperature," *Journal of Physics and Chemistry of Solids*, vol. 151, p. 109928, 2021.

[22] S. Debnath, "X-ray diffraction analysis for the determination of elastic properties of zinc-doped manganese spinel ferrite nanocrystals ($Mn_{0.75}Zn_{0.25}Fe_2O_4$), along with the determination of ionic radii, bond lengths, and hopping lengths," *Journal of Physics and Chemistry of Solids*, vol. 134, pp. 105–114, 2019.

[23] I. Soibam, "Preparation and studies of electrical properties of cobalt substituted Li-Zn ferrites by sol-gel auto combustion method," *Indian Journal of Physics*, vol. 83, no. 3, pp. 285–290, 2009.

[24] H. Rietveld, "Line profiles of neutron powder-diffraction peaks for structure refinement," *Acta Crystallographica*, vol. 22, no. 1, pp. 151–152, 1967.

[25] L. Lutterotti, "Maud: A Rietveld analysis program designed for the internet and experiment integration," *Acta Crystallographica Section A*, vol. 56, p. s54, 2000.

[26] H. M. Rietveld, "A profile refinement method for nuclear and magnetic structures," *Journal of applied Crystallography*, vol. 2, no. 2, pp. 65–71, 1969.

[27] B. H. Toby, "R factors in Rietveld analysis: How good is good enough?," *Powder Diffraction*, vol. 21, no. 1, pp. 67–70, 2006.

[28] P. Saengkwamsawang, P. Katekaew, and A. Klinbumrung, "Dissolution-recrystallization growth and structural characteristics of facile decomposition-processed $NiFe_2O_4$ octahedrons," *Journal of Crystal Growth*, vol. 633, p. 127648, 2024.

[29] Z. L. Wang, "Transmission electron microscopy of shape-controlled nanocrystals and their assemblies," *The Journal of Physical Chemistry B*, vol. 104, no. 6, pp. 1153–1175, 2000.

[30] H. Müller-Buschbaum, "The crystal chemistry of AM2O4 oxometallates," *Journal of Alloys and Compounds*, vol. 349, no. 1, pp. 49–104, 2003.

[31] A. Bajorek, "Microstructural and magnetic characterization of $Ni_{0.5}Zn_{0.5}Fe_2O_4$ ferrite nanoparticles," *Journal of Physics and Chemistry of Solids*, vol. 129, pp. 1–21, 2019.

[32] M. M. Mubasher, M. Hassan, L. Ali, Z. Ahmad, M. A. Imtiaz, and K. Nadeem, "Comparative study of frequency-dependent dielectric properties of ferrites MFe_2O_4 (M= Co, Mg, Cr and Mn) nanoparticles," *Applied Physics A*, vol. 126, no. 5, p. 334, 2020.

[33] E. Pieczyńska, "Thermo-optical parameters of amorphous aC: N: H layers," *Acta Physica Polonica A*, vol. 126, no. 6, pp. 1241–1245, 2014.

[34] Z. Zhou, "$NiFe_2O_4$ nanoparticles formed in situ in silica matrix by mechanical activation," *Journal of Applied Physics*, vol. 91, no. 9, pp. 6015–6020, 2002.

[35] A. Sangeetha, K. V. Kumar, and G. N. Kumar, "Effect of annealing temperature on the structural and magnetic properties of NiFe2O4 nanoferrites," *Advances in Materials Physics and Chemistry*, vol. 7, no. 02, pp. 19–27, 2017.

[36] S. Patange, "Elastic properties of nanocrystalline aluminum substituted nickel ferrites prepared by co-precipitation method," *Journal of Molecular Structure*, vol. 1038, pp. 40–44, 2013.

[37] H. Zaki and H. Dawoud, "Far-infrared spectra for copper–zinc mixed ferrites," *Physica B: Condensed Matter*, vol. 405, no. 21, pp. 4476–4479, 2010.

[38] K. A. Kumar and R. Bhowmik, "Micro-structural characterization and magnetic study of $Ni_{1.5}Fe_{1.5}O_4$ ferrite synthesized through coprecipitation route at different pH values," *Materials Chemistry and Physics*, vol. 146, no. 1–2, pp. 159–169, 2014.

[39] R. S. Yadav, "Effects of annealing temperature variation on the evolution of structural and magnetic properties of $NiFe_2O_4$ nanoparticles synthesized by starch-assisted sol–gel auto-combustion method," *Journal of Magnetism and Magnetic Materials*, vol. 394, pp. 439–447, 2015.

[40] G. Burns, *Solid State Physics*. New York: Academic Press Inc., 1985.

[41] L. K. Babu and Y. R. Reddy, "A novel thermal decomposition approach for the synthesis and properties of superparamagnetic nanocrystalline $NiFe_2O_4$ and its antibacterial, electrocatalytic properties," *Journal of Superconductivity and Novel Magnetism*, vol. 33, no. 4, pp. 1013–1021, 2020.

[42] Q. Lu, "Electronic structure and optical properties of spinel structure $Zn_{1-x}Ni_xAl_2O_4$ nanopowders synthesized by sol–gel method," *Chemical Physics Letters*, vol. 772, p. 138582, 2021.

[43] Y. Keereeta, S. Thongtem, and T. Thongtem, "Enhanced photocatalytic degradation of methylene blue by $WO_3/ZnWO_4$ composites synthesized by a combination of microwave-solvothermal method and incipient wetness procedure," *Powder Technology*, vol. 284, pp. 85–94, 2015.

[44] M. M. Naik, "Effect of aluminium doping on structural, optical, photocatalytic and antibacterial activity on nickel ferrite nanoparticles by sol–gel auto-combustion method," *Journal of Materials Science: Materials in Electronics*, vol. 29, pp. 20395–20414, 2018.

[45] D. Dorranian and A. F. Eskandari, "Effect of laser fluence on the characteristics of ZnO nanoparticles produced by laser ablation in acetone," *Molecular Crystals and Liquid Crystals*, vol. 607, no. 1, pp. 1–12, 2015.

[46] F. S. Tehrani, "Structural, magnetic, and optical properties of zinc- and copper-substituted nickel ferrite nanocrystals," *Journal of Superconductivity and Novel Magnetism*, vol. 25, no. 7, pp. 2443–2455, 2012.

[47] G. Branković, "Fractal approach to AC impedance spectroscopy studies of ceramic materials," *Journal of Electroceramics*, vol. 7, pp. 89–94, 2001.

[48] S. Holm, "Time domain characterization of the Cole-Cole dielectric model," *Journal of Electrical Bioimpedance*, vol. 11, no. 1, pp. 101–105, 2020.